New Journal of Physics
The open-access journal for physics

Theory and experimental verification of Kapitza–Dirac–Talbot–Lau interferometry

Klaus Hornberger[1,2], Stefan Gerlich[2], Hendrik Ulbricht[2,3], Lucia Hackermüller[2,4], Stefan Nimmrichter[2], Ilya V Goldt[5], Olga Boltalina[5,6] and Markus Arndt[2,7]

[1] Arnold Sommerfeld Center for Theoretical Physics, Ludwig-Maximilians-Universität München, Theresienstraße 37, 80333 München, Germany
[2] Faculty of Physics, University of Vienna, Boltzmanngasse 5, A-1090 Wien, Austria
[3] School of Physics and Astronomy, University of Southampton, UK
[4] Johannes Gutenberg-Universität Mainz, Staudingerweg 7, 55099 Mainz, Germany
[5] Department of Chemistry, Moscow State University, Moscow 119992, Russia
[6] Department of Chemistry, Colorado State University, Fort Collins, CO 80523, USA
E-mail: markus.arndt@univie.ac.at

New Journal of Physics **11** (2009) 043032 (23pp)
Received 31 January 2009
Published 27 April 2009
Online at http://www.njp.org/
doi:10.1088/1367-2630/11/4/043032

Abstract. Kapitza–Dirac–Talbot–Lau interferometry (KDTLI) has recently been established for demonstrating the quantum wave nature of large molecules. A phase space treatment permits us to derive closed equations for the near-field interference pattern, as well as for the moiré-type pattern that would arise if the molecules were to be treated as classical particles. The model provides a simple and elegant way to account for the molecular phase shifts related to the optical dipole potential as well as for the incoherent effect of photon absorption at the second grating. We present experimental results for different molecular masses, polarizabilities and absorption cross sections using fullerenes and fluorofullerenes and discuss the alignment requirements. Our results with C_{60} and C_{70}, $C_{60}F_{36}$ and $C_{60}F_{48}$ verify the theoretical description to a high degree of precision.

[7] Author to whom any correspondence should be addressed.

Contents

1. Introduction

The quantum wave nature of matter has become a corner stone of physics over many decades, and current interest in de Broglie interferometry with electrons [1]–[3], neutrons [4], atoms [5, 6] and molecules [7, 8] ranges from demonstrating fundamental quantum phenomena to advanced applications in the materials sciences and in quantum metrology. All these experiments require optical elements for the coherent manipulation of matter waves. While clean solid surfaces and bulk crystal structures are well adapted to the diffraction of electrons and neutrons with de Broglie wavelengths in the range of 1–1000 pm, it is often necessary to tailor the beam splitters, lenses and wave guides to the specific particle properties in atomic and molecular applications.

For complex molecules, nanofabricated gratings were demonstrated to act as beam splitters for far-field diffraction [7, 9] and near-field interferometry [10]. However, these experiments pointed already to the importance of van der Waals interactions between the molecules and the diffraction grating, which largely exceeds the effect observed with atoms [11] because of the high molecular polarizability and their comparatively low velocity. The interaction time with a 500 nm thick grating amounts to only 5 ns at a beam velocity of 100 m s^{-1}, and yet the matter-wave phase shift can attain the value of several radians in the center of the slit opening. The interaction effect gets even stronger close to the slit walls, to a degree that the wave front distortion can no longer be described by a phase shift alone [12]. For particles with increasing polarizability this strong influence of the grating interaction leads to prohibitive requirements on the velocity, as discussed in [13]. It is therefore appealing to replace material gratings by structures made of light, which offer the additional advantage of being indestructible, highly transparent and easy to tune and modulate.

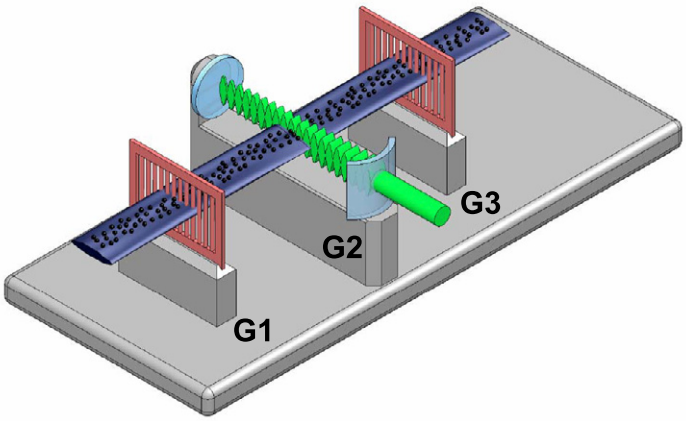

Figure 1. Setup of the KDTLI: it consists of two material nanostructures ($G1$, $G3$) and a standing light wave ($G2$). The latter is realized by a cylindrical lens focusing a 532 nm laser beam onto a mirror. The three structures ($G1$, $G2$, $G3$) have the same period of 266 nm and are separated equidistantly by 105 mm. For detection, the third grating ($G3$) is shifted in small steps over the molecular interference pattern. The transmitted molecules are detected in a quadrupole mass spectrometer.

Bragg diffraction of *free electrons* at a standing light field was already proposed by Kapitza and Dirac in 1933 [14], but nearly seventy years passed before the idea was experimentally implemented [15]. In contrast to that, the first optical phase grating for atoms was already realized in 1983 [16, 17] when a standing laser light field was tuned near to an atomic resonance in order to perform Raman–Nath ('thin grating') diffraction of a supersonic sodium beam. A related investigation [18] then focused on *atomic diffraction* in the Bragg regime ('thick grating'). These ideas were later extended to atom diffraction [19] and interferometry [20, 21], also to the time domain [22]–[24], and to the manipulation of *Bose–Einstein* condensates [25, 26].

The working principle of all phase grating examples is the same: a coherent laser beam creates a periodic pattern of the electrical field amplitude. This couples to the particle's polarizability, shifts the energy and thus imprints a phase pattern on the transmitted matter-wave beam. Its evolution into a modulated particle density distribution can then be observed further downstream.

Large, hot molecules in thermal beams often exhibit broad absorption lines. Light will therefore mainly couple in a non-resonant fashion. However, for most molecules one can still find a suitable range of wavelengths where the light–molecule coupling allows one to imprint a local matter-wave phase shift of the order of $\Delta\Phi = \pi$.

The first application of optical phase gratings to *large, hot molecules* was demonstrated with C_{60} in a far-field diffraction experiment [27]. The combination with near-field diffraction was suggested in [28] and recently implemented in a Kapitza–Dirac–Talbot–Lau interferometer (KDTLI) [13], as shown in figure 1.

The general idea behind the KDTLI design has been described elsewhere [13, 28]: A first absorptive mechanical structure, $G1$, (in the present experiment $d = 266$ nm) prepares the

required spatial coherence for illuminating the optical phase grating, *G*2. Quantum interference then explains the appearance of an approximate self-image of *G*2 at the position of the third mask *G*3. This molecular density pattern is scanned by shifting *G*3 across the beam, while counting the transmitted molecules as a function of the mask position. This scheme was exploited to perform quantum interference experiments up to extended polyatomic molecular chains [13] and to determine electrical molecular properties [29, 30].

In the present paper, we now provide a refined theoretical description of KDTL interference, putting special emphasis on the proper incorporation of the influence of photon absorption in the second grating. We give a closed expression for both the quantum interference visibility and the fringe contrast one would expect if a classical moiré description were correct. We then compare this to the measured interference curves of C_{60} and C_{70}, which are in nearly perfect agreement with the quantum result. We also apply the KDTL concept to studying the fluorofullerenes $C_{60}F_{36}$ and $C_{60}F_{48}$. This allows us to assess the influence of mass, absorption cross section and optical polarizability on the interference of large particles. In comparison to earlier Talbot–Lau experiments [31], the new KDTLI now also allows us to establish a significantly improved fringe contrast.

2. Theory of the KDTLI

The KDTLI is a derivative of the standard Talbot–Lau interferometer [5, 10, 32, 33], obtained by substituting the central grating mask with the optical phase grating created by a standing laser beam. In the simplest configuration all gratings, material and optical, have the same grating period d, given by one half of the laser wavelength, $d = \lambda_L/2$. The passage of the matter-wave beam through each grating may thus transfer integer multiples of the grating momentum $p_d = h/d = 2h/\lambda_L$ to the transverse motion in the beam. These different diffraction orders interfere further downstream, leading to a resonant enhancement at integer multiples of the Talbot length $L_T = d^2/\lambda_{dB}$, which is determined by the de Broglie wave length λ_{dB} of the molecules (which ranges between 1 and 5 pm in our experiment). The emerging interference pattern at the position of the third grating thus displays a strong dependence of the interference fringe visibility on λ_{dB}, as determined by the longitudinal velocity v_z of the beam.

Unlike with material gratings, in the KDTLI we must also consider the possibility that one or more laser photons are scattered or absorbed, while the molecule traverses the standing light wave. The associated incoherent transfer of transverse momentum may strongly blur the fringe pattern. If the absorption is followed by an immediate isotropic reemission process, this causes an additional transverse momentum shift of up to the photon momentum h/λ_L. However, in many large molecules the absorbed photon energy gets stored for a rather long time, either in metastable excited states or, after rapid internal conversion, in the vibrational degrees of freedom, which do not decay over the time scale of the experiment. The associated transverse momentum transfer is then an integer multiple of the photon momentum h/λ_L, corresponding to one half of the grating momentum p_d. An odd number of net photon momenta will thus kick the molecular wave such that the fringes get blurred maximally, whereas an even number will have a much weaker effect. We note that related physics has already been described in the context of far-field diffraction [34] and Mach–Zehnder interferometry [35] with atoms before.

In order to describe the interplay of coherent diffraction and the incoherent effect of photon absorption, we follow the phase space formulation of Talbot–Lau interference based on the Wigner function, as presented in [36]. It provides a transparent representation of all relevant

coherent and incoherent phenomena, and it permits us to calculate the quantum interference pattern on an equal footing with the possible moiré-type structures, which might arise already due to classical mechanics in this setup. This comparison with the classical description is required if one wants to establish that the observed fringe pattern in a molecule interference experiment is caused by a genuine quantum interference effect.

2.1. The light-grating interaction

We start by collecting the necessary ingredients for describing the effects of a light grating on the motion of a beam of polarizable particles. Taking the direction of the particle beam as the z-axis, we set the retro-reflected, basic Gaussian laser mode in the perpendicular x-direction. The time-averaged intensity of the standing light wave is then given by

$$I(x, y, z) = \frac{8P}{\pi w_y w_z} \exp\left(-\frac{2y^2}{w_y^2} - \frac{2z^2}{w_z^2}\right) \sin^2\left(\pi \frac{x}{d}\right), \tag{1}$$

where w_y and w_z denote the laser beam waists in the vertical and the longitudinal direction, and P is the laser power. In the following, we assume the particle beam height to be sufficiently small compared to w_y, such that the dependence on the vertical y-direction can be safely neglected. This is approximately the case in our experiment, see below.

The standing light field will in general induce dispersive and absorptive forces on a molecule. The first type, due to the conservative optical dipole force, is described by the potential

$$V(x, z) = -\frac{2\pi \alpha_\omega}{c} I(x, 0, z), \tag{2}$$

where α_ω is the real part of the polarizability of the particle at the laser frequency $\omega = 2\pi c/\lambda_L$ (related to the polarizability in SI units by $\alpha_{SI}(\omega) = 4\pi\varepsilon_0\alpha_\omega$).

Treating the effect of the grating potential in the eikonal approximation, a traversing quantum wave acquires a position-dependent phase shift, which is calculated by integrating the potential along a straight line,

$$\phi(x) = -\frac{1}{\hbar}\int_{-\infty}^{\infty} V(x, v_z t)\mathrm{d}t = \phi_0 \sin^2\left(\pi \frac{x}{d}\right). \tag{3}$$

The maximal shift

$$\phi_0 = 8\sqrt{2\pi}\,\frac{\alpha_\omega}{\hbar c}\,\frac{P}{w_y v_z}, \tag{4}$$

thus increases linearly with the optical polarizability and laser power, and it is inversely proportional to the molecule velocity v_z. The justification of this eikonal approximation and its range of applicability are discussed in some detail in [12]. As shown there, it is well justified for the molecular masses and polarizabilities accessible with the current experimental setup.

The second type of momentum exchange between the light and the molecules is the radiation pressure force due to photon absorption. The molecules used in the present experiment are sufficiently large and internally complex that it is justified to both ignore any reemission and to take the absorption cross section constant even after the absorption of several photons. In this case, all absorption events can be described as being independent and as only determined by the absorption cross section σ_{abs} at the laser frequency $\omega = 2\pi\nu$. This cross section can often be

related to the imaginary part of the polarizability using Mie theory, $\sigma_{\rm abs} = 4\pi\omega/c \times {\rm Im}(\alpha(\omega))$, but we will treat $\sigma_{\rm abs}$ as an independent parameter in the following.

The photon absorption rate is determined by the incident photon flux $I(x,z)/h\nu$ and $\sigma_{\rm abs}$,

$$\Gamma(x,z) = \frac{\sigma_{\rm abs}}{h\nu} I(x,z). \tag{5}$$

Below, the radiation pressure effect on the molecular beam will be described by the position-dependent mean number of absorbed photons. The latter is obtained from the photon absorption rate, in analogy to the eikonal approximation, by a straight integration along the longitudinal motion of the molecule,

$$\bar{n}(x) = \int_{-\infty}^{\infty} \Gamma\,(x, v_z t)\,{\rm d}t = n_0\,\sin^2\left(\pi\frac{x}{d}\right). \tag{6}$$

The maximum mean number of absorbed photons n_0 is found in the antinodes of the standing light wave, and it is given by

$$n_0 = \frac{8}{\sqrt{2\pi}}\frac{\sigma_{\rm abs}\lambda_{\rm L}}{hc}\frac{P}{w_y v_z}. \tag{7}$$

The values of ϕ_0 and n_0 defined in (4) and (7) are the two key parameters describing the molecule–light interaction, and they will appear in the closed formula for the quantum interference visibility below.

Classical description. We note that the momentum-changing effect of photon absorptions does not differ in the quantum and the classical description of the molecular motion. On the other hand, the classical effect of the optical dipole force due to the potential (2) should be treated in analogy to the eikonal approximation of the quantum case. This is done in terms of the momentum kick $Q(x)$ obtained by integrating the dipole force along the same straight line as in the eikonal treatment [36],

$$Q(x) = -\int_{-\infty}^{\infty} \frac{\partial V}{\partial x}\,(x, v_z t)\,{\rm d}t = \frac{\pi\hbar}{d}\phi_0\,\sin\left(2\pi\frac{x}{d}\right), \tag{8}$$

with ϕ_0 from (4). (The $\hbar$ in the prefactor cancels Planck's constant in ϕ_0 rendering the equation classical.)

As we will see below, the spatially periodic focusing of classical particles due to the dipole potential (8) may result in a regular molecule pattern behind the light grating, though distinctly different from the quantum prediction. To perform the quantum and the classical calculations it is useful to formulate the effect of the grating passage in a common framework, the Wigner–Weyl phase space representation.

2.2. Phase space formulation of the light-grating transformation

The most important part in describing the KDTL interference is the transformation of the particle beam state as it passes the second grating. We consider the Wigner function

$$w(x,p) = \frac{1}{2\pi\hbar}\int {\rm d}s\, {\rm e}^{2\pi {\rm i} s p/\hbar}\langle x - \frac{s}{2}|\rho|x + \frac{s}{2}\rangle \tag{9}$$

of the transverse quantum state of motion ρ of the molecular beam [36]–[38], where x and p denote the position and momentum coordinates in phase space, and we first assume the longitudinal velocity of the molecules to be given by a definite value v_z.

After passing an arbitrary grating in eikonal approximation, the transformed beam state can always be written as [36]

$$w'(x,\,p) = \int \mathrm{d}p_0\; T\,(x,\,p-p_0)\; w(x,\,p_0). \tag{10}$$

That is, the momentum dependence of the quasi-probability distribution gets modified by a convolution, while its position dependence is at most affected by a multiplication.

Let us now discuss the grating transformation for an arbitrary, d-periodic distribution of the light intensity. We first assume that there is no absorption, $\sigma_{\mathrm{abs}} = 0$, so that the grating transformation is entirely coherent. The phase shift $\phi(x)$ then relates the wave function ψ in front of the grating to the one behind, $\psi'(x) = \exp(\mathrm{i}\phi(x))\psi(x)$. In phase space representation, this coherent transformation is described by the convolution kernel [36]

$$T_{\mathrm{coh}}(x,\,p) = \frac{1}{2\pi\hbar}\int \mathrm{d}s\; \mathrm{e}^{\mathrm{i}ps/\hbar}\; \exp\left[\mathrm{i}\phi\left(x-\frac{s}{2}\right) - \mathrm{i}\phi\left(x+\frac{s}{2}\right)\right]. \tag{11}$$

Noting the periodicity of $\phi(x)$ we define the Fourier coefficients

$$b_j = \frac{1}{d}\int_{-d/2}^{d/2} \exp(\mathrm{i}\phi(x))\mathrm{e}^{-2\pi\mathrm{i}jx/d}\mathrm{d}x, \tag{12}$$

so that the coherent kernel takes the form

$$T_{\mathrm{coh}}(x,\,p) = \sum_{j,m\in\mathbb{Z}} b_j b^*_{j-m}\; \exp\left(2\pi\,\mathrm{i}m\frac{x}{d}\right)\delta\left(p-\left(j-\frac{m}{2}\right)p_d\right). \tag{13}$$

This is a periodic comb of delta-functions separated by integer multiples of the grating momentum $p_d = h/d$. It serves to populate the different diffraction orders in (10) as the quantum wave passes the grating.

In a second limiting case, we now consider the grating transformation for a vanishing dipole force, $\alpha_\omega = 0$, but maintain a finite absorption cross section. It is reasonable to assume that the final detection efficiency of the beam particles is practically independent of the number of absorbed photons. In this case, their motional state gets effectively replaced by a statistical mixture whose components differ by momentum translations of integer multiples of the photon momentum $h/\lambda_{\mathrm{L}} = p_d/2$. These multiples correspond to the difference in the number of photons absorbed from the left and from the right side. We denote as $\mathrm{Prob}(k;\,x)$ the position-dependent probability distribution for the exchange of $k \in \mathbb{Z}$ net photon momenta. The mixture can then be written in phase space representation as $w'(x,\,p) = \sum_k \mathrm{Prob}(k;\,x)w(x,\,p-kp_d/2)$. That is, the statistical redistribution of the momenta due to photon absorption is described by the incoherent kernel

$$T_{\mathrm{abs}}(x,\,p) = \sum_{k\in\mathbb{Z}} \mathrm{Prob}(k;\,x)\delta\left(p-k\frac{p_d}{2}\right). \tag{14}$$

Expanding the periodic position dependence of $\mathrm{Prob}(k;\,x)$ in a Fourier series,

$$\mathrm{Prob}(k;\,x) = \sum_{j\in\mathbb{Z}} P_j^{(k)}\mathrm{e}^{2\pi\mathrm{i}jx/d}, \tag{15}$$

it takes the form

$$T_{\mathrm{abs}}(x,\,p) = \sum_{k,j\in\mathbb{Z}} \mathrm{e}^{2\pi\mathrm{i}jx/d}\,P_j^{(k)}\delta\left(p-k\frac{p_d}{2}\right). \tag{16}$$

Let us now specify the probability distribution (15) in terms of the mean number of absorbed photons $\bar{n}(x)$. Since the absorption events are taken to be statistically independent the probability $\mathrm{Prob}(k;x)$ for the net gain of k photon momenta is given by

$$\mathrm{Prob}(k;x) = \sum_{n=0}^{\infty} \mathrm{Prob}(k|n) \frac{\bar{n}^n(x)}{n!} \mathrm{e}^{-\bar{n}(x)}. \tag{17}$$

Here, $\bar{n}(x)$ is the position-dependent mean number of photon absorptions characterizing the Poissonian distribution and $\mathrm{Prob}(k|n)$ is the probability for the net transfer of k photon momenta towards one side, conditioned on the absorption of exactly n photons. Since absorptions from the left and from the right occur with the same probability in a standing light wave, the latter is given by the distribution of a one-dimensional, balanced random walk with n steps,

$$\mathrm{Prob}(k|n) = \frac{1}{2^n} \begin{cases} \binom{n}{(k+n)/2}, & \text{if } n+k \text{ even}, \\ 0, & \text{otherwise}. \end{cases} \tag{18}$$

In order to perform the average over the Poissonian photon distribution in (17) we first calculate the characteristic function of (18) by means of the binomial theorem

$$\mathrm{X}(\xi|n) = \sum_{k\in\mathbb{Z}} \exp(-2\pi \mathrm{i} k\xi)\, \mathrm{Prob}(k|n) = [\cos(2\pi\xi)]^n . \tag{19}$$

The characteristic function of the averaged distribution (17) thus takes the simple form

$$\begin{aligned} \mathrm{X}(\xi;x) &= \sum_{n=0}^{\infty} \frac{[\bar{n}(x)\cos(2\pi\xi)]^n}{n!} \exp(-\bar{n}(x)) \\ &= \exp\{-\bar{n}(x)[1-\cos(2\pi\xi)]\}. \end{aligned} \tag{20}$$

The inverse Fourier transform of (20) yields the required probability (17) in terms of the mean number of absorbed photons,

$$\mathrm{Prob}(k;x) = \exp(-\bar{n}(x))\, I_k(\bar{n}(x)), \tag{21}$$

where the $I_n(x)$ are modified Bessel functions of the first kind.

So far, the integral kernels T_{coh} and T_{abs}, which describe the coherent and the incoherent part of the light-grating interaction, were discussed separately, see equations (13) and (16). For realistic molecules the dispersive and the dissipative light forces coexist, and their combined contribution is described in the eikonal approximation by a single transformation (10), whose kernel is given by the convolution of T_{coh} and T_{abs},

$$T(x,p) = \int \mathrm{d}q\; T_{\mathrm{coh}}(x, p-q) T_{\mathrm{abs}}(x,q). \tag{22}$$

Classical description. As an advantage of the phase space formulation, it is easy to describe in the same framework how the molecules would move if they were classical particles. One merely replaces the Wigner function by the classical phase space distribution, which is a proper probability density. Both the quantum Wigner function and the classical phase space distribution experience the same shearing transformation as they evolve freely between the optical elements, see the discussion in [36]. Also the passage through a grating can be expressed in the same form (10) in both cases, though the integral kernels differ of course. The classical kernel due to the dipole force takes the form (10)

$$T_{\mathrm{cl}}(x,p) = \delta(p - Q(x)), \tag{23}$$

where $Q(x)$ is the classical momentum kick of equation (8). The effect of a photon absorption, on the other hand, is described by the same kernel (14) as in the quantum case, since it effects the same momentum change on the motional state, irrespective whether the center-of-mass motion is described by classical or quantum dynamics. To obtain the combined effect of dispersive and absorptive light forces, one can again concatenate the two transformations.

2.3. Evaluating the KDTL effect

We are now in the position to calculate the interference pattern expected for the KDTLI in the same spirit as it was done for purely coherent grating interactions in [36]. The final beam state is obtained by applying the appropriate sequence of free evolution and grating transformations to its Wigner function. Starting with a spatially completely incoherent but monochromatic beam in front of the first grating one thus obtains the spatial density distribution in front of the third grating by a final integration over the momentum variable,

$$w_3(x) \propto \sum_{k\in\mathbb{Z}} \int \mathrm{d}x_0\, \mathrm{d}p\; T_1(x_0)\, T_{\mathrm{coh}}\left(x - \frac{p}{p_z}L, 2p - \frac{x-x_0}{L}p_z - k\frac{p_d}{2}\right) \mathrm{Prob}\left(k, x - \frac{p}{p_z}L\right). \tag{24}$$

Here L is the distance between the gratings and $T_1(x_0) \in \{0, 1\}$ denotes the binary function, which specifies the transmission of the first material grating. The latter serves to imprint a density modulation onto the beam, thus creating the required spatial coherence downstream at the light grating. We characterize the material grating mask by the Fourier coefficients

$$A_j := \frac{1}{d}\int_{-d/2}^{d/2} T_1(x)\mathrm{e}^{-2\pi \mathrm{i} jx/d}\mathrm{d}x, \tag{25}$$

where d is the common period of all gratings.

In order to evaluate the interference pattern (24) it is now convenient to define the coherent *Talbot–Lau coefficients* in terms of the Fourier coefficients (12), which describe the phase shift due to the optical dipole potential,

$$B_m(\xi) := \sum_{j\in\mathbb{Z}} b_j b_{j-m}^*\, \exp\left(-2\pi\mathrm{i}\left[j - \frac{m}{2}\right]\xi\right). \tag{26}$$

The incoherent effect of the light grating is best accounted for through the characteristic coefficients associated with the Fourier coefficients of the periodic probability distribution (15). They are given by

$$\chi_j(\xi) := \sum_{k\in\mathbb{Z}} P_j^{(k)}\, \exp(-2\pi\mathrm{i}k\xi) \tag{27}$$

and they serve to define the general Talbot–Lau coefficients, which include the effect of absorption,

$$\hat{B}_m(\xi) := \sum_{n\in\mathbb{Z}} B_n(\xi)\chi_{m-n}\left(\frac{1}{2}\xi\right). \tag{28}$$

The factor $1/2$ in (28) reflects the fact a single photon has a momentum that equals one half of the grating momentum p_d. As one expects, the convolution (28) reduces to the coherent expression (26) if absorption can be neglected, i.e. for $\chi_m(\xi) = \delta_{m,0}$.

Inserting the Fourier expressions (13) and (15) into (24) the integrations can now be carried out by retaining the resonant contributions. This yields the interference pattern in terms of the coefficients (25) and (28),

$$w_3(x) = \sum_{\ell\in\mathbb{Z}} A_\ell^* \hat{B}_{2\ell} \left(\ell \frac{L}{L_\mathrm{T}}\right) \exp\left(2\pi \mathrm{i}\ell \frac{x}{d}\right). \tag{29}$$

Here $L_\mathrm{T} = d^2/\lambda_\mathrm{db}$ denotes the *Talbot length*, which gives the characteristic length scale for near-field interference.

One records the beam intensity behind the third gratings as a function of the lateral position x_s, $S(x_s) \propto \int \mathrm{d}x\, T_3(x - x_s) w_3(x)$. Since the first and third gratings are identical in our experiments, $T_1(x) = T_3(x)$, the expected interference signal reads

$$S(x_s) = \sum_{\ell\in\mathbb{Z}} \left(A_\ell^*\right)^2 \hat{B}_{2\ell} \left(\ell \frac{L}{L_\mathrm{T}}\right) \exp\left(2\pi \mathrm{i}\ell \frac{x_s}{d}\right). \tag{30}$$

Classical description. Using the same general formalism as above the classical result is obtained by replacing the Wigner function by the classical phase space density and the kernel $T_\mathrm{coh}(x, p)$ in (24) by its classical counterpart (23). The evaluation of the corresponding moiré-type density distribution suggests to introduce the *classical coefficients*

$$C_m(\xi) = \frac{1}{d} \int_{-d/2}^{d/2} \mathrm{d}x\ \exp\left(-2\pi \mathrm{i}m \frac{x}{d}\right) \exp\left(-2\pi \mathrm{i} \frac{Q(x)}{p_d} \xi\right). \tag{31}$$

They are the classical analogue of the Talbot–Lau coefficients (26), but clearly lacking an interference phase factor. Performing the same steps as above, the classical prediction for the signal behind the third grating thus assumes a form analogous to (30),

$$S_\mathrm{cl}(x_\mathrm{s}) = \sum_{\ell\in\mathbb{Z}} \left(A_\ell^*\right)^2 \hat{C}_{2\ell} \left(\ell \frac{L}{L_\mathrm{T}}\right) \exp\left(2\pi \mathrm{i}\ell \frac{x_\mathrm{s}}{d}\right), \tag{32}$$

where $L_\mathrm{T} = d^2 m v_z/h$, with m the molecular mass and v_z their longitudinal velocity. Note that Planck's constant appearing in L_T cancels against the one from $p_d = h/d$ showing up in (31); it is kept here to maintain the close analogy with the quantum result. Like in (28), the possibility of photon absorption is accounted for in (32) by a convolution with the characteristic coefficients (27),

$$\hat{C}_m(\xi) = \sum_n C_n(\xi) \chi_{m-n}\left(\frac{1}{2}\xi\right). \tag{33}$$

2.4. Closed expressions for the sinusoidal light grating

The results obtained so far are valid for gratings with arbitrary eikonal phase shifts and momentum kick distributions. We now focus on the complex light grating of our experiment, as defined by the intensity distribution (1). Their special form will yield closed formulae for the Talbot–Lau coefficients (28) and their classical analogues (33).

The sinusoidal x dependence of the phase shift (3) implies that the Fourier coefficients are determined by the integer Bessel functions,

$$b_m = (-\mathrm{i})^m\, \mathrm{e}^{\mathrm{i}\phi_0/2} J_m\left(\frac{\phi_0}{2}\right). \tag{34}$$

The summation for the coherent Talbot–Lau coefficient (26) can be carried out by means of Graf's addition theorem for Bessel functions [39]. This leads to

$$B_m(\xi) = J_m\left(-\phi_0 \sin(\pi\xi)\right) \tag{35}$$

indicating that all the Talbot–Lau coefficients are real.

It is instructive to compare this to the corresponding coefficients (31) of the classical formulation. It follows immediately from (8) that they are given by

$$C_m(\xi) = J_m(-\pi\phi_0\xi). \tag{36}$$

Comparing the quantum expression (35) and the classical one (36), we see that both coefficients assume the same limiting form if the Talbot parameter ξ is much smaller than unity. They do, however, strongly deviate for $\xi \geqslant 1$. The distinguishing quality of the *quantum wave* coefficients (35) is their periodicity in ξ, which gives rise to the characteristic Talbot–Lau recurrences. *Classical* particles show no such recurrences since their coefficients (36) exhibit no periodicity in ξ.

We move on to evaluate the characteristic coefficients (27). There is no obvious way to express the Fourier coefficients P_n^k from equation (15) in closed form. However, the coefficients $\chi_m(\xi)$ can be expressed as the Fourier transform of the characteristic function (20) with respect to position,

$$\chi_m(\xi) = \int_{-1/2}^{1/2} \mathrm{d}\tau \ \exp\left(-2\pi i m\tau\right) \mathrm{X}(\xi, \tau d). \tag{37}$$

Due to the sinusoidal position dependence of the mean photon number (6) the integration can be carried out, yielding a modified Bessel function,

$$\chi_m(\xi) = \exp\left(-n_0 \sin^2(\pi\xi)\right) I_m\left(n_0 \sin^2(\pi\xi)\right). \tag{38}$$

The Talbot–Lau coefficients in the presence of absorption can now be obtained by performing the summation in (28). This can be done using an addition theorem for mixtures of regular and modified Bessel functions, which can be derived from Graf's addition theorem. It reads, for $u, v \in \mathbb{R}$, $u \neq v$,

$$\left(\frac{v-u}{v+u}\right)^{n/2} J_n\left(-\mathrm{sgn}(u+v)\sqrt{v^2-u^2}\right) = \sum_{k\in\mathbb{Z}} I_{k+n}(u)\, J_k(v) \tag{39}$$

and yields a real number also for $|v| < |u|$ since $J_n(\mathrm{i}u) = \mathrm{i}^n I_n(u)$.

Using (35) and (37), and noting $J_{-n}(z) = J_n(-z)$, we thus obtain the general coefficients of the KDTLI, which incorporate the effect of photon absorption. They are given by

$$\hat{B}_m(\xi) = \exp\left(-\zeta_{\mathrm{abs}}(\xi)\right)\left(\frac{\zeta_{\mathrm{coh}}(\xi)-\zeta_{\mathrm{abs}}(\xi)}{\zeta_{\mathrm{coh}}(\xi)+\zeta_{\mathrm{abs}}(\xi)}\right)^{m/2} J_m\left(-\mathrm{sgn}\left[\zeta_{\mathrm{abs}}(\xi)+\zeta_{\mathrm{coh}}(\xi)\right]\sqrt{\zeta_{\mathrm{coh}}^2(\xi)-\zeta_{\mathrm{abs}}^2(\xi)}\right). \tag{40}$$

Here, the coherent diffraction effect of the dipole force is described by the function

$$\zeta_{\mathrm{coh}}(\xi) = \phi_0 \sin(\pi\xi) \tag{41}$$

and the incoherent effect of absorption is accounted for by

$$\zeta_{\mathrm{abs}}(\xi) = n_0 \sin^2\left(\frac{\pi}{2}\xi\right). \tag{42}$$

Classical description. The coefficients for the classical motion (33) can be obtained the same way starting from (36) and (37). Given the relation between the classical and the quantum coefficients (36) and (35), it is not surprising that the $\hat{C}_m(\xi)$ assume a similar form as the $\hat{B}_m(\xi)$ in (40). The only difference is that $\zeta_{\rm coh}(\xi)$ is replaced by

$$\zeta_{\rm cl}(\xi) = \phi_0 \pi \xi, \tag{43}$$

which lacks the periodicity in the Talbot parameter ξ shown by (41).

2.5. Discussion of the theoretical results

2.5.1. The fringe visibility. Using the above results it is now easy to calculate the expected quantum interference pattern (30) and the corresponding classical prediction (32). However, for the parameters of our experiment the patterns are well described by a sine curve so that it is sufficient to characterize the experimentally observed pattern by the contrast of a sinusoidal fit. This sinusoidal fringe visibility can be calculated as the ratio of the first two Fourier coefficients of the fringe pattern, $\mathcal{V} = 2|S_1/S_0|$.

We denote by f the open fraction (i.e. the ratio between the single slit width and the grating period) of the first and the third grating, so that the grating coefficients (25) are given by $A_\ell = f\,\mathrm{sinc}(\ell\pi f)$. The quantum fringe visibility then takes the form

$$\mathcal{V}_{\rm qm} = 2\,\mathrm{sinc}^2(\pi f)\left|\hat{B}_2\left(\frac{L}{L_{\rm T}}\right)\right| \tag{44}$$

with the coefficient $\hat{B}_2$ given by (40).

Similarly, the fringe pattern expected form classically moving molecules has a visibility $\mathcal{V}_{\rm cl} = 2\,\mathrm{sinc}^2(\pi f)|\hat{C}_2(L/L_{\rm T})|$ which is obtained from (44), if we replace the function of coherent diffraction $\zeta_{\rm coh}(\xi)$ by the classical function $\zeta_{\rm cl}(\xi)$ defined in equation (43).

2.5.2. Comparing the classical and quantum predictions. Let us now see how the quantum interference pattern differs from the fringe pattern expected from classically evolving particles. Figure 2 compares the corresponding visibilities $\mathcal{V}_{\rm qm}$ and $\mathcal{V}_{\rm cl}$ as one varies the de Broglie wave length or velocity. The latter is specified by $L/L_{\rm T} = L/d^2 \times \lambda_{\rm dB}$ both in the quantum and the classical case. For the material gratings we assume an open fraction of $f = 0.42$, like in our experiment.

The most important feature of the quantum result (top row in figure 2) is that the visibilities are generally much greater than the classical calculation (bottom row). They also display more structure if the strength of the dipole potential increases (from left column to right column), a consequence of the intricate near-field interference process. At first sight, it may seem surprising that a fringe visibility would be observed at all in this setup if the molecules were moving as classical particles. This is due to a moiré-type effect, where the light grating acts as a periodic structure of lenses focusing the classical trajectories. Note that these classical visibilities are systematically suppressed in the 'quantum regime' $L/L_{\rm T} \gg 1$. They coincide with the quantum result only in the 'classical limit' $L/L_{\rm T} \to 0$ of a vanishing de Broglie wavelength.

One also observes in figure 2 that the visibility peaks are affected rather differently by the possibility of photon absorption. Close to even multiples of $L/L_{\rm T}$ the classical contrast remains essentially unaffected by absorption, while the quantum visibility vanishes identically at all integer multiples of $L/L_{\rm T}$ in the absence of absorption. It is a curious result of our theory that a

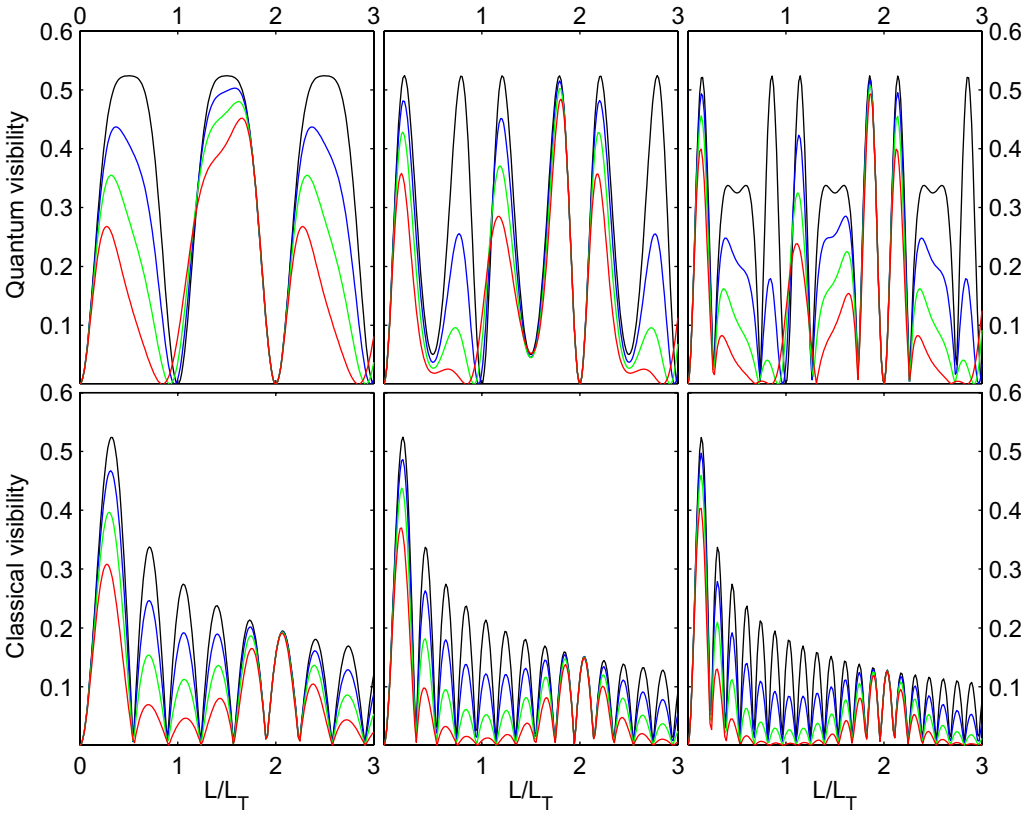

Figure 2. Fringe visibilities as obtained from the quantum (top) and classical (bottom) description of the molecular motion in a KDTLI. The abscissa value L/L_{T} is proportional to the molecular de Broglie wave length; it scales as v_z^{-1}, also in the classical case. The material gratings are chosen to have an open fraction of $f = 0.42$ [13]. The maximal optical phase shift increases from $\phi_0 = 3$ (left panel), $\phi_0 = 5$ (middle) to $\phi_0 = 7$ (right). Each line in each panel describes the fringe visibility for a specific maximal mean number of absorbed photons n_0, which is given, from the top to the bottom lines, by $n_0/\phi_0 = 0$, 10, 25 and 50%. The quantum and the classical fringe visibilities differ markedly both in their value and in their functional dependence, except for the limit of high velocities, i.e. small de Broglie wave lengths $L/L_{\mathrm{T}} \to 0$. The visibility peaks are strongly affected by photon absorption.

certain fringe pattern can be observed even if the dipole force can be neglected compared with photon absorption, $\phi_0 \to 0$. The quantum and the classical predictions coincide in this case, and one expects a sinusoidal visibility given by

$$\mathcal{V}_{\mathrm{abs}} = 2\,\mathrm{sinc}^2(\pi f)\,\exp\left[-\zeta_{\mathrm{abs}}\left(\frac{L}{L_{\mathrm{T}}}\right)\right] I_2\left[\zeta_{\mathrm{abs}}\left(\frac{L}{L_{\mathrm{T}}}\right)\right]. \tag{45}$$

It is greatest if the maximum mean number of absorbed photons equals $n_0 = 4.65$. The visibility then amounts to $\max(\mathcal{V}_{\mathrm{abs}}) = 0.236 \times \mathrm{sinc}^2(\pi f)$, i.e. a value of 24% cannot be exceeded by this effect.

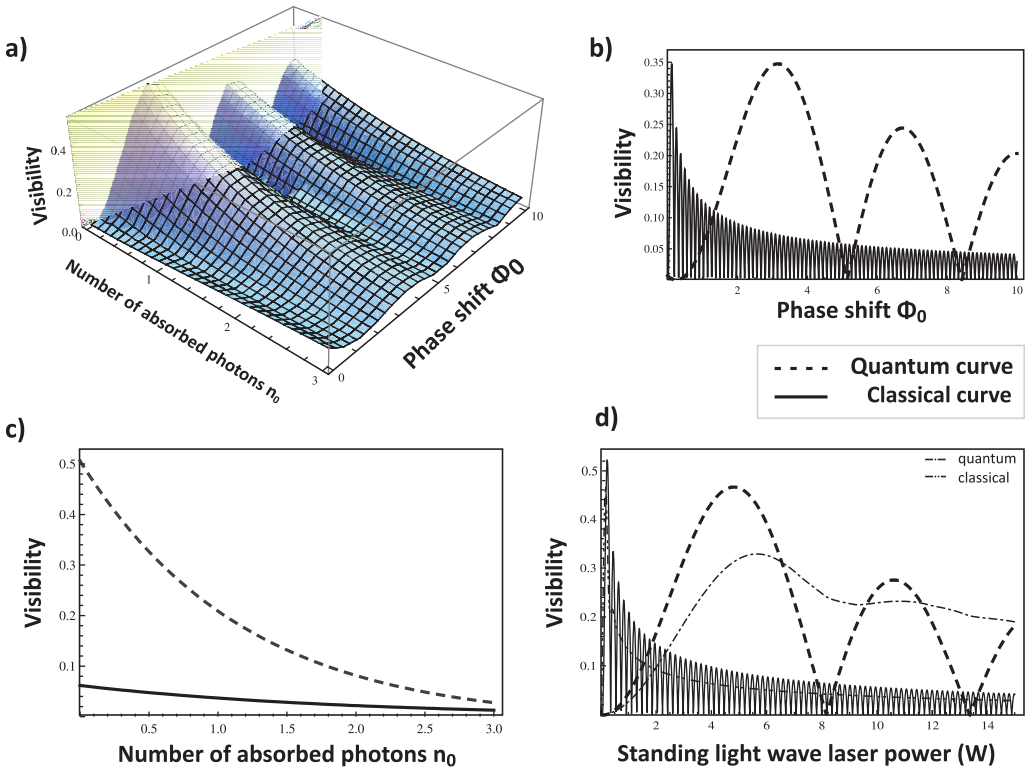

Figure 3. Interference visibility for a fixed value of $L/L_T = 8.5$ and $f = 0.42$ for C_{60}, which corresponds to a velocity of 97 m s^{-1}. Panel (a) shows the quantum interference visibility as a function of Φ_0 and n_0. Panels (b)–(d) display cuts through this figure, along with the smaller classical fringe visibility (solid lines). (b) is the cut along $n_0 = 0.5$, (c) shows the cut for fixed $\Phi_0 = 2.7$ and (d) is a cut along the surface shown in (a), which corresponds to a linear increase in the power of the light grating according to equations (4) and (7). Also shown in (d) is the effect of a velocity distribution $\Delta v/v = 10\%$ on the quantum (dashed dotted curve) and classical (dash double dotted curve) visibility.

Finally, figure 3 shows for a fixed value of L/L_T how the visibilities depend on the molecular properties, which are summarized in the dipole force phase ϕ_0 and the absorption number n_0. We choose $L/L_T = 8.5$, which corresponds to C_{60} fullerenes at a velocity of 97 m s^{-1}. One observes that at fixed velocity the parameter dependence is less complicated than the wave length dependence of figure 2. Since the molecular velocity is easy to control this implies that KDTL interference can be used to measure the molecular polarizability and the absorption cross section by varying the intensity of the light grating [13, 29, 30].

So far, the molecular beam was assumed to be characterized by a fixed longitudinal velocity v_z. The case of a finite velocity spread is easily incorporated by averaging the interference patterns of the monochromatic theory with the measured velocity distribution in the beam. This also applies to the sinusoidal visibilities, since the zeroth Fourier component of the interference pattern is independent of the velocity.

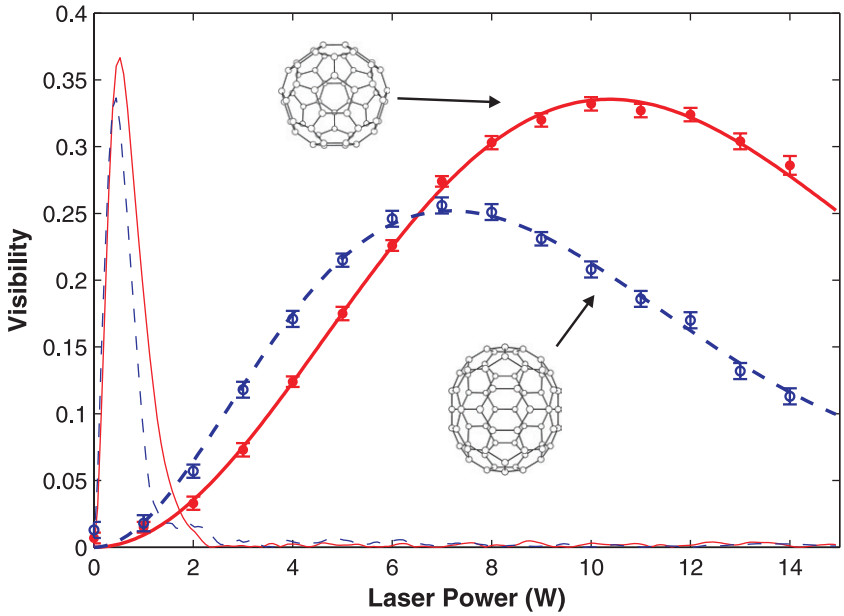

Figure 4. Power dependence of the interference contrast for the fullerenes C_{60} (filled circles) and C_{70} (open circles). The points represent the weighted average of three consecutive measurements, the error bars depict one standard deviation. Bold lines display the quantum expectations, obtained by weighting equation (44) with the experimentally observed velocity distribution and fitting α and σ_0. The corresponding classical expectations are shown as thin lines. The solid lines identify the theoretical predictions for C_{60}, whereas the dashed lines correspond to C_{70}.

3. Verification of the model using fullerenes and fluorofullerenes

In a first experiment a mixture of the fullerenes C_{60} (720 amu) and C_{70} (840 amu) was co-sublimated in a thermal source (see figure 1) at a temperature of 910 K. By alternating the setting of the detecting quadrupole mass spectrometer between the masses of the two molecules, the interference patterns of either species were recorded, one after the other, before the laser power was shifted to the next point in the series. This way, we assured that the standing light wave conditions were the same for both molecules. The result is shown in figure 4. Each data point represents the weighted average of three consecutive measurements, where the confidence intervals of the individual sine fits serve as weights. The single patterns were recorded over four full sine periods with ten points per period and two seconds integration time per point. The mean count rates per second amounted to 740 for C_{60} and 505 for C_{70}.

The velocity of the particles was selected by limiting their path to the associated free flight parabola in the Earth's gravitational field [40]. This yields an approximately Gaussian velocity distribution. The mean velocities in the experiment were determined to be 202 m s^{-1} for C_{60} and 194 m s^{-1} for C_{70} with velocity spreads of 27 and 25%, respectively ($\Delta v/v$, full-width at half-maximum (FWHM)). The interferometer setup is characterized by a grating period of $d = 266$ nm (corresponding to a laser wave length of 532 nm), a grating separation of $L = 105$ mm, a molecular beam height of about 200 μm and a beam width of about 1 mm. The slit widths are assumed to be 85 nm in $G1$ and 110 nm in $G3$.

Both visibility curves reproduce the quantum expectations accurately (bold lines, equation (30)), while being in distinctive disagreement with the classical prediction (thin lines, equation (32)). We emphasize that the present result signifies a noticeable improvement over previous measurements [13]. We attribute the enhanced interference contrast mainly to further improvement of the highly critical adjustment of the machine as outlined in section 4.

From the perfect accordance with the theory we also deduce that decoherence due to collisions with particles of the background gas is negligible in our current experiments. Following [41] we estimate an effective cross section for collisions of $\sigma_{\mathrm{eff}} = 4.2 \times 10^{-17}\,\mathrm{m}^2$ for C_{70}. The experiment is conducted under pressures below 10^{-8} mbar, which results in a mean free path of more than 17 m. This corresponds to a reduction of the effective visibility of $\mathcal{V}_{\mathrm{eff}} > 0.98\,\mathcal{V}_0$. Since the effective collisional cross section is mainly governed by the polarizability of the molecule rather than its geometrical size, an even smaller reduction of the visibility can be expected for the other species discussed in this paper.

We also observe, and again in good agreement with our model, that the fringe contrast of the more absorptive C_{70} decays significantly more rapidly than the contrast of C_{60} when we increase the laser power. The increasing number of absorbed photons fills in the interference minima with shifted interference curves, thus washing out the accumulated interference pattern.

It may come as a surprise that, in spite of the higher absorption cross section, C_{70} exhibits actually a higher interference contrast than C_{60} at lower laser powers. This can be explained by the optical polarizability which, according to our present measurement, amounts to $\alpha_{\mathrm{AC}} = 114\,\text{Å}^3$ for C_{70} and is thus 31% higher than for C_{60}. This results in a larger phase shift in the optical grating and thus leads to a shift of the entire curve to the left in figure 4.

The experiment was repeated in two additional and separate runs with the fluorofullerenes $C_{60}F_{36}$ and $C_{60}F_{48}$. The $C_{60}F_{36}$ sample was synthesized by the method described in [42] with a compositional purity of $>95\%$ as determined by mass spectrum analysis. It contains two major isomers of C_3 and C_1 symmetry in the approximate ratio 2 : 1, as well as one minor isomer of T symmetry (about 5%) [43]. The three isomers of $C_{60}F_{36}$ show very similar polarizabilities, ranging between 62 and 65 Å, according to calculations performed with Gaussian [44]. Depending on the specific isomer, $C_{60}F_{36}$ may possess a dipole moment of upto 1.2 Debye. The sample of $C_{60}F_{48}$ was purchased from Professor L Sidorov, Moscow. The synthesis and characterization were done according to Boltalina and Galeva [45]. $C_{60}F_{48}$ is formed predominantly as a single isomer of D_3 symmetry, with the minor isomer of S_6 symmetry comprising about 5% [43]. For both isomers of $C_{60}F_{48}$ the simulations yield virtually identical polarizabilities and no dipole moment. Both fluorofullerene samples were produced before the year 2003 but remained intact compounds over this period, as proven by mass spectra.

It is noteworthy that an earlier experiment in a pure Talbot–Lau configuration succeeded already with $C_{60}F_{48}$ but at limited contrast [31]. The present setup, however, substantially outperforms its predecessor: the more sophisticated KDTLI scheme, an improved count rate and a better vibration insulation with respect to the earlier experiment allowed us for the first time to achieve the full expected quantum contrast for both $C_{60}F_{36}$ and $C_{60}F_{48}$, as shown in figure 5. The larger error bars with respect to the C_{60}–C_{70} measurement are mainly a consequence of the lower count rates of only 60 and 75 per second for $C_{60}F_{36}$ and $C_{60}F_{48}$, respectively. The temperature was kept at 590 K for both molecules.

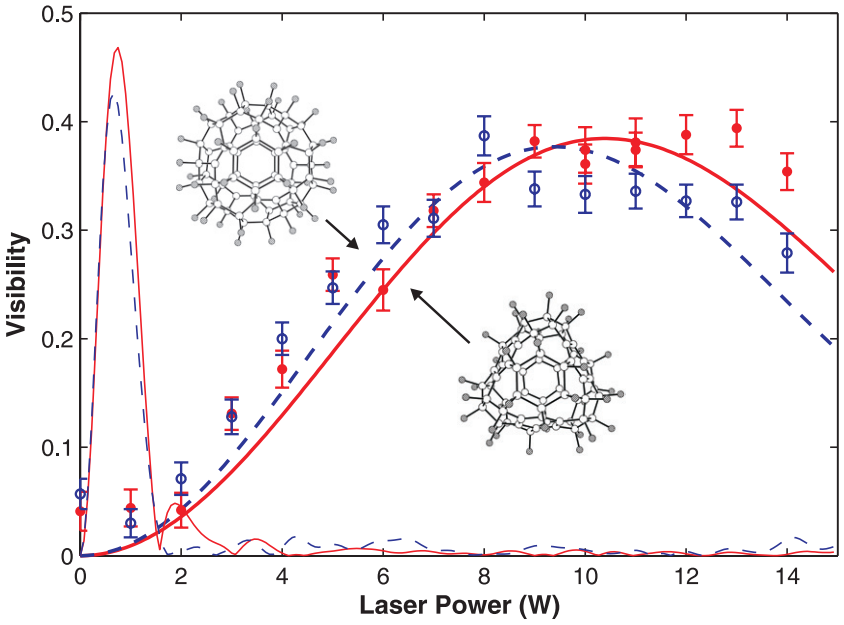

Figure 5. Power dependence of the interference contrast for the fluorofullerenes $C_{60}F_{36}$ (filled circles) and $C_{60}F_{48}$ (open circles). The circles represent the weighted average of three consecutive measurements, the error bars depict one standard deviation of the shot noise. Bold lines display the quantum expectations. The values used for the parameters α and σ_0 correspond to a best fit and are depicted in table 1. Classical expectations are shown as thin lines. Solid lines correspond to $C_{60}F_{36}$ and dashed lines to $C_{60}F_{48}$.

The recorded velocities for $C_{60}F_{36}$ and $C_{60}F_{48}$ were of 130 and 116 m s^{-1} with velocity spreads of 16 and 18%, respectively. Although smaller velocities tend to make the experiment more susceptible to vibrations, drifts and misalignment, no significant drop of the measured visibility below the theoretical expectation was observed.

In table 1, we compare the optical properties of all four particles that were extracted from a best fit of the quantum curves to the experimental data. All values are in good agreement with the parameters determined in independent experiments [29, 46] and with molecular simulations carried out using Gaussian. The remarkably small statistical errors indicate that our method offers the capacity for high precision metrology experiments with heavy molecules. The accuracy is, however, currently limited by the systematic errors, which are primarily governed by the accuracy of the measurement of the power ($\pm$5%) and the waist ($\pm$10%) of the diffracting laser beam.

The decrease in polarizability from C_{60} to $C_{60}F_{48}$ is in good agreement with the observation that fluorinated molecules in general show a reduced polarizability-to-mass ratio and correspondingly lower inter-molecular binding, lower sublimation enthalpies and higher vapor pressures at a given temperature [50]. It is also important to see that the fluorine shell reduces the absorption cross section at the wavelength of the diffracting laser beam to a negligible value. Our measurement thus allows us to extract information about the effect of fluorination on the electronic properties of fullerenes.

Table 1. Molecular parameters as derived from the best fit of the theory including statistical and systematic errors. The data are in very good agreement with the values provided by literature, where published, or with simulations performed with Gaussian [44]. The simulation yields slightly different values for the three conformers of $C_{60}F_{36}$, ranging between 62 and 65 Å^3. Note that the published and calculated values represent *static* polarizabilities, whereas our experiment yields the *optical* polarizability at the laser wavelength of 532 nm.

Molecule	C_{60}	C_{70}	$C_{60}F_{36}$	$C_{60}F_{48}$
$\sigma_{abs}(10^{-22}\,m^2)$	$2.8 \pm 0.3 \pm 0.3$	$24.9 \pm 1.1 \pm 2.7$	<0.6	<0.5
$\alpha_{opt}(Å^3)$ (Exp.)	$87.1 \pm 0.5 \pm 9.7$	$114.2 \pm 0.9 \pm 12.7$	$60.3 \pm 1.0 \pm 6.7$	$60.1 \pm 0.8 \pm 6.7$
$\alpha_{stat}(Å^3)$ (Lit.)	$88.9 \pm 0.9 \pm 5.1$ [46]	$108.5 \pm 2.0 \pm 6.2$ [46]	62–65 [44]	63 [44]
$\alpha(Å^3)$ (Lit.)	89.2 [47]	109.2 [47]	—	—
$\alpha(Å^3)$ (Lit.)	90 [48]	118.4 [48]	—	—
$\alpha(Å^3)$ (Lit.)	98.2 [49]	122.6 [49]	—	—

4. Alignment requirements for precision experiments

Matter-wave interferometry with large molecules operates with de Broglie wavelengths in the range of a few picometers and grating periods as small as a few hundred nanometers. As a result of this, the interferometer alignment has to be considered carefully. The following section is therefore devoted to a short assessment of the constraints on the experimental precision.

4.1. Equality of grating periods

If the first two gratings have only slightly different lattice periods, the interference pattern spacing will not match the period of the third mask and the contrast will be reduced. A period mismatch as small as one per mille leads already to half a fringe shift between slit one and five hundred.

In practice, all grating periods must be, on average, equal to better than 0.05 nm, i.e. about the diameter of a hydrogen atom. This condition enters both the choice of the grating manufacturing process and the alignment of the yaw angle for all gratings. Modern photolithography and etching procedures allow to reach this level of precision. The gratings for our experiments were produced by Dr Tim Savas at MIT and 'nm^2' Inc, Cambridge, Massachusetts and independently checked by Ibsen Photonics, Denmark. The gratings were fabricated to be 0.3 nm wider than the period of the standing light wave in order to allow for later yaw adjustments.

4.2. Transverse grating shifts and grating roll angles

The lateral position Δx_i of all gratings relative to each other determines the final location of the fringe pattern. For Talbot–Lau interferometry, we can define a phase of the near-sinusoidal interferogram, which is determined by the relative shift of the molecular density maxima with regard to the openings of the third grating. For geometrical reasons this phase is

determined by [51]

$$\phi = k_{\mathrm{d}}(\Delta x_1 - 2\Delta x_2 + \Delta x_3) \tag{46}$$

with $k_{\mathrm{d}} = 2\pi/d$. In a symmetrical setup such as ours, with $L_1 = L_2$, the prefactor of the first and third gratings must be equal, while the second grating's shift enters twice. Molecules passing the gratings at different heights y_i will effectively see different transverse grating shifts $\Delta x_i = \alpha_i\, y_i$ if element i is rolled by the angle α_i. Although a simple phase shift will not reduce the fringe visibility, an integration over many height-dependent shifts does. If we neglect gravity, we can assume the second grating to define the reference angle, $\alpha_2 = 0$, and study the influence of rolling G_1 by α_1 and G_3 around α_3. In the paraxial limit, the total signal $\overline{S}(x)$ behind the third grating is then

$$\overline{S}(x) = \frac{1}{h_{\mathrm{s}} h_{\mathrm{d}}} \int_{-h_{\mathrm{s}}/2}^{h_{\mathrm{s}}/2} \int_{-h_{\mathrm{d}}/2}^{h_{\mathrm{d}}/2} \mathrm{d}y_{\mathrm{s}}\, \mathrm{d}y_{\mathrm{d}}\, S(x, k_{\mathrm{d}}\Delta x_1 + k_{\mathrm{d}}\Delta x_3) \tag{47}$$

$$= S_0 \left(1 + \mathcal{V}\, \sin(x)\, \mathrm{sinc}\left(k_{\mathrm{d}} h_{\mathrm{s}} \alpha_1'\right) \mathrm{sinc}\left(k_{\mathrm{d}} h_{\mathrm{d}} \alpha_3'\right)\right), \tag{48}$$

where the transmission function S is parametrized as a sine wave of amplitude S_0 with visibility $\mathcal{V}$ and height-dependent phase shifts x_1 and x_3. We denote $\alpha_1' = \alpha_1 L_2 (L_1 + L_2 + L_3)/(L_1 L_{\mathrm{tot}}) + \alpha_3 L_3 / L_{\mathrm{tot}}$, $\alpha_3' = \alpha_1 L_0 L_2/(L_1 L_{\mathrm{tot}}) + \alpha_3 (L_0 + L_1 + L_2)/L_{\mathrm{tot}}$ with $L_{\mathrm{tot}} = (L_0 + L_1 + L_2 + L_3)$ and all distances as shown in figure 6.

From equation (48) we see that rolling G_1 and G_3 reduces the fringe visibility in a sinc-shaped functional dependence. The alignment becomes increasingly important for smaller grating constants and more extended molecular beams. In our experiment, the first zero of the sinc curve appears for a roll angle of around 0.65 mrad.

In addition to shifting the phase, rolling also affects the effective grating constant. If one of the gratings is rolled with respect to the others its projected period increases by $d_{\mathrm{eff}} = d/\cos(\alpha) \simeq d + d\alpha^2/2 + O(\alpha^4)$ (see figure 6). If we require the relative period change not to exceed $(d_{\mathrm{eff}} - d)/d = 10^{-4}$, the roll angle has to be kept aligned to within 10 mrad.

4.3. Longitudinal grating shifts

The semiclassical picture in figure 6(a) shows that the interference pattern is also blurred when the third mask is moved relative to the second grating by the distance $\pm\Delta L$. For symmetry reasons, the same is true for a movement of $G1$. The contrast is severely reduced when the blur $D = d/2$ is as wide as half a grating period. We see that this condition is met when

$$\frac{D}{\Delta L} = \frac{d/2}{\Delta L} = \frac{Nd}{2L}, \tag{49}$$

where N is the number of grating slits illuminated by the molecular beam. We thus derive the *length-balance criterion*

$$\frac{\Delta L}{L} < \frac{1}{N}. \tag{50}$$

When 4000 lines are illuminated, as in our experiments, we have to balance the distances to better than 25 μm. This is already comparable with the waist of the diffracting laser beam. This intuitive condition is consistent with a complementary and more rigorous treatment using Wigner functions [12].

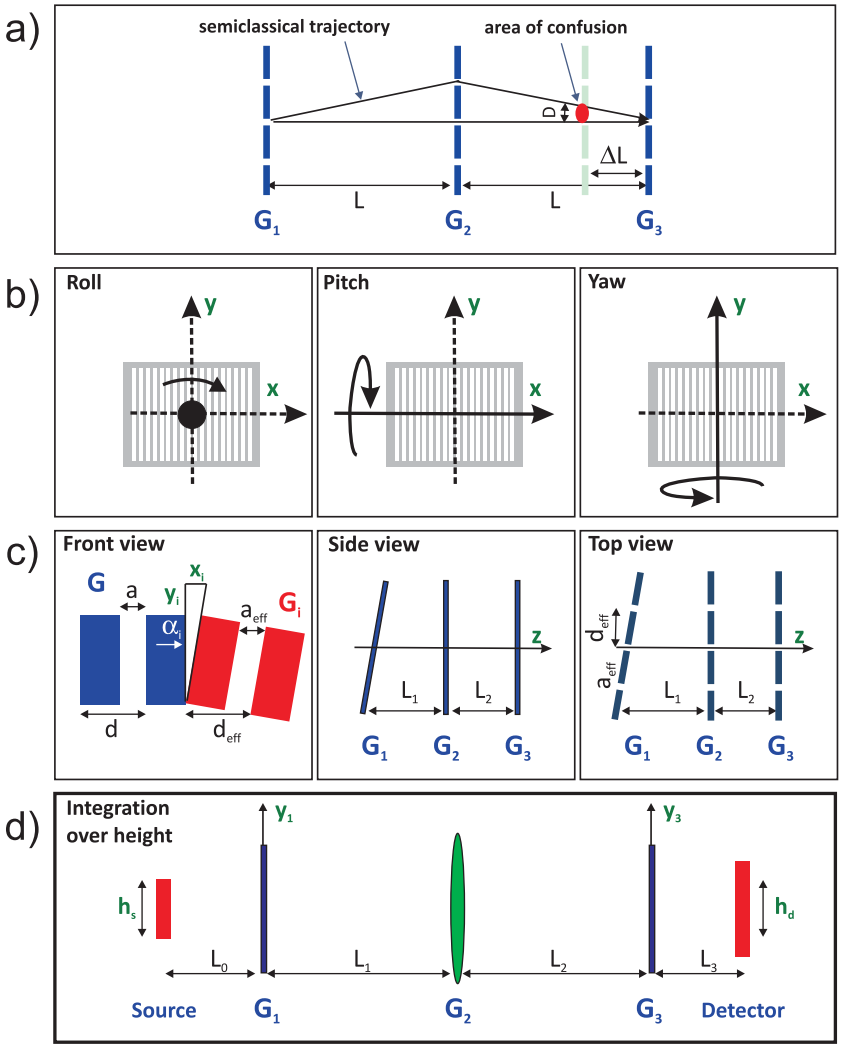

Figure 6. Illustration of the alignment considerations. (a) An imbalance of grating separations leads to blurred interferences. (b) and (c) Illustration of the grating's motion during roll, pitch and yaw. (d) Distances relevant for the assessment of grating roll: molecules can pass the gratings at different altitudes and different transverse positions if the gratings are rolled with regard to each other. The height of the first velocity selection slit is $h_s = 150\,\mu$m, whereas the third one is restricted to $h_d = 200\,\mu$m. The distance between the source and G_1 is $L_0 = 150$ cm, whereas the spacing between G_3 and the detector is $L_3 = 250$ mm. The grating separation amounts to $L_1 = L_2 = 105$ mm. The beam width of about 1 mm is sufficient to illuminate nearly 4000 grating openings.

4.4. Grating pitch

The effect of forward or backward tilting a single grating, i.e. to add a *pitch*, is to introduce a height-dependent imbalance in the grating separation. The pitch must be compatible with the requirement of equation (50). If the beam height is h and the forward pitch is measured by the angle θ then the arm lengths are balanced as long as $\Delta z = h\theta \ll L/N$. For our experiment

with $h = 100\,\mu$m, $L = 105$ mm and $N = 4000$, this corresponds to 250 mrad. This condition can easily be met.

4.5. Grating yaw

To first order, the argument for grating pitch also holds for grating yaw. However, yaw also changes the slit's effective period as well as their effective open width. Under a yaw of angle ϕ the grating constant shrinks like $d_y = \cos(\phi)d \approx d - \phi^2 d/2$. Similarly to the roll-related period change we derive the condition $\phi < 10$ mrad.

Finally, we have to include the effective reduction of the open slit width if the grating is turned: the openings shrink because of the finite wall thickness b to $a_{\text{eff}} = a - b\tan\phi$. A reduction of the open fraction in the first or third grating is important as it tends to increase the fringe visibility, while decreasing the count rate at the same time. A variation by 10% in visibility is already rather clearly noticeable, leading to the constraint: $0.1 \geqslant (a_{\text{eff}} - a)/a = -(b/a)\tan\phi$. For $a = 90$ nm and $b = 190$ nm, we thus find a limit of $\phi = 47$ mrad for the maximally allowed yaw angle in our experiments.

For the second grating a different reasoning applies: the optical grating is about 20 μm thick along the direction of the molecular beam, therefore we have to make sure that no molecule crosses a sizeable fraction of the standing light wave period transversely. Since the period is as small as 266 nm the condition imposes a limit on both the angle of incidence and the divergence angle of the molecular beam: $\phi \leqslant 0.1 \times 266/20\,000 \simeq 1$ mrad.

5. Conclusions

Our experiment combines the virtues of near-field interferometry with the advantages of optical manipulation. Compared with far-field diffraction of collimated beams, near-field interferometry provides higher signal throughput at the expense of increased alignment requirements. As discussed in this paper, the experimental challenges are non-negligible but manageable with reasonable effort. Optical phase gratings allow us to operate with highly polarizable molecules, which would otherwise acquire prohibitively large van der Waals phases by interacting with the walls of material gratings.

The KDTLI is very well described using a Wigner function approach, which facilitates in particular the inclusion of grating transformations and momentum exchange in the interferometer. The model is in excellent agreement with the experiments, even for particles as complex as $C_{60}F_{36}$ and $C_{60}F_{48}$. Actually the KDTLI allowed us to observe much improved contrast compared with earlier pure Talbot–Lau experiments with the same particles [31].

This instrument and its theoretical description are now a good basis for continuing the quest for the ultimate mass and complexity limits of matter-wave interferometry. In addition, it has proven to be useful for a number of relevant measurements of molecular properties, such as optical polarizabilities and absolute optical absorption cross sections [29, 30, 52]. Interestingly the rich internal structure of complex molecules, including electric dipole moments or magnetic moments, structural properties etc, can be ignored unless they either modify the optical polarizability or unless we introduce additional field gradients or collisions [41], which allows these properties to be coupled separately [46].

Acknowledgment

We thank the Austrian science foundation FWF for support within the projects Z149 Wittgenstein and the doctoral program W1210 CoQuS. We also acknowledge financial support by the MIME project within the ESF Eurocore EuroQUASAR program. K H is supported by the DFG within the Emmy Noether program.

References

[1] Tonomura A 1987 *Rev. Mod. Phys.* **59** 639–69
[2] Batelaan H 2007 *Rev. Mod. Phys.* **79** 929–41
[3] Sonnentag P and Hasselbach F 2007 *Phys. Rev. Lett.* **98** 200402
[4] Rauch H and Werner A 2000 *Neutron Interferometry: Lessons in Experimental Quantum Mechanics* (Oxford: Oxford University Press)
[5] Berman P R 1997 *Atom Interferometry* (New York: Academic)
[6] Cronin A D, Schmiedmayer J and Pritchard D E 2009 *Rev. Mod. Phys.* at press (arXiv:0712.3703)
[7] Arndt M, Nairz O, Voss-Andreae J, Keller C, der Zouw G V and Zeilinger A 1999 *Nature* **401** 680–2
[8] Arndt M and Hornberger K 2009 *Proc. Int. School of Physics on Quantum Coherence in Solid State Physics* Course CLXXI, IOP at press (arXiv:0903.1614)
[9] Bruehl R, Guardiola R, Kalinin A, Kornilov O, Navarro J, Savas T and Toennies J P 2004 *Phys. Rev. Lett.* **92** 185301
[10] Brezger B, Hackermüller L, Uttenthaler S, Petschinka J, Arndt M and Zeilinger A 2002 *Phys. Rev. Lett.* **88** 100404
[11] Grisenti R E, Schöllkopf W, Toennies J P, Hegerfeldt G C and Köhler T 1999 *Phys. Rev. Lett.* **83** 1755
[12] Nimmrichter S and Hornberger K 2008 *Phys. Rev.* A **78** 023612
[13] Gerlich S *et al* 2007 *Nat. Phys.* **3** 711–5
[14] Kapitza P L and Dirac P A M 1933 *Proc. Camb. Phil. Soc.* **29** 297–300
[15] Freimund D L, Aflatooni K and Batelaan H 2001 *Nature* **413** 142–3
[16] Moskowitz P E, Gould P L, Atlas S R and Pritchard D E 1983 *Phys. Rev. Lett.* **51** 370–3
[17] Gould P L, Ruff G A and Pritchard D E 1986 *Phys. Rev. Lett.* **56** 827–30
[18] Martin P J, Oldaker B G, Miklich A H and Pritchard D E 1988 *Phys. Rev. Lett.* **60** 515–8
[19] Steane A, Szriftgiser P, Desbiolles P and Dalibard J 1995 *Phys. Rev. Lett.* **74** 4972–5
[20] Rasel E M, Oberthaler M K, Batelaan H, Schmiedmayer J and Zeilinger A 1995 *Phys. Rev. Lett.* **75** 2633–7
[21] Giltner D M, McGowan R W and Lee S A 1995 *Phys. Rev. Lett.* **75** 2638–41
[22] Cahn S B, Kumarakrishnan A, Shim U, Sleator T, Berman P R and Dubetsky B 1997 *Phys. Rev. Lett.* **79** 784–7
[23] Turlapov A, Tonyushkin A and Sleator T 2005 *Phys. Rev.* A **71** 043612
[24] Tonyushkin A and Sleator T 2006 *Phys. Rev.* A **74** 053615
[25] Ovchinnikov Y, Muller J, Doery M, Vredenbregt E, Helmerson K, Rolston S and Phillips W 1999 *Phys. Rev. Lett.* **83** 284–7
[26] Deng L, Hagley E W, Wen J, Trippenbach M, Band Y, Julienne P S, Simsarian J E, Helmerson K, Rolston S L and Phillips W D 1999 *Nature* **398** 218
[27] Nairz O, Brezger B, Arndt M and Zeilinger A 2001 *Phys. Rev. Lett.* **87** 160401
[28] Brezger B, Arndt M and Zeilinger A 2003 *J. Opt. B: Quantum Semiclass. Opt.* **5** S82–9
[29] Hackermüller L, Hornberger K, Gerlich S, Gring M, Ulbricht H and Arndt M 2007 *Appl. Phys.* B **89** 469–73
[30] Gerlich S, Gring M, Ulbricht H, Hornberger K, Tüxen J, Mayor M and Arndt M 2008 *Angew. Chem. Int. Edn. Engl.* **47** 6195–8
[31] Hackermüller L, Uttenthaler S, Hornberger K, Reiger E, Brezger B, Zeilinger A and Arndt M 2003 *Phys. Rev. Lett.* **91** 090408

[32] Patorski K 1989 *Progress in Optics XXVII* ed E Wolf (Amsterdam: Elsevier) pp 2–108
[33] Clauser J F and Li S 1994 *Phys. Rev.* A **49** R2213
[34] Pfau T, Spälter S, Kurtsiefer C, Ekstrom C and Mlynek J 1994 *Phys. Rev. Lett.* **73** 1223–6
[35] Chapman M S, Hammond T D, Lenef A, Schmiedmayer J, Rubenstein R A, Smith E and Pritchard D E 1995 *Phys. Rev. Lett.* **75** 3783–7
[36] Hornberger K, Sipe J E and Arndt M 2004 *Phys. Rev.* A **70** 053608
[37] Hillery M, O'Connell R F, Scully M O and Wigner E P 1984 *Phys. Rep.* **106** 121
[38] Englert B, Miniatura C and Baudon J 1994 *J. Physique* II **4** 2043–59
[39] Erdelyi A *et al* 1954 *Tables of Integral Transforms* vol 1 (New York: McGraw-Hill)
[40] Arndt M, Nairz O, Petschinka J and Zeilinger A 2001 *C. R. Acad. Sci., Paris* IV **2** 1–5
[41] Hornberger K, Uttenthaler S, Brezger B, Hackermüller L, Arndt M and Zeilinger A 2003 *Phys. Rev. Lett.* **90** 160401
[42] Boltalina O V, Borschevskii A Y, Sidorov L N, Street J M and Taylor R 1996 *Chem. Commun.* 529–530
[43] Popov A A, Senyavin V M, Boltalina O V, Seppelt K, Spandl J, Feigerle C S and Compton R N 2006 *J. Phys. Chem.* A **110** 8645–52
[44] Frisch M *et al* 2003 *Gaussian 03W, V6.0* (Pittsburgh, PA: Gaussian, Inc.)
[45] Boltalina O V and Galeva N A 2000 *Usp. Khim.* **69** 661–74
[46] Berninger M, Stéfanov A, Deachapunya S and Arndt M 2007 *Phys. Rev.* A **76** 013607
[47] Guha S, Menendez J, Page J and Adams G 1996 *Phys. Rev.* B **53** 13106
[48] Eklund P, Rao A, Wang Y, Zhou P, Wang K, Holden J, Dresselhaus M and Dresselhaus G 1995 *Thin Solid Films* **257** 211
[49] Sohmen E, Fink J and Krätschmer W 1992 *Z. Phys.* B **86** 87
[50] Boltalina O V, Markov V Y, Borschevskii A Y, Galeva N A, Sidorov L N, Gigli G and Balducci G 1999 *J. Phys. Chem.* B **103** 3828–32
[51] Oberthaler M K, Bernet S, Rasel E M, Schmiedmayer J and Zeilinger A 1996 *Phys. Rev.* A **54** 3165–76
[52] Nimmrichter S, Hornberger H, Ulbricht H and Arndt M 2008 *Phys. Rev.* A **78** 063607